

Direct jet reconstruction in $p + p$ and $\text{Cu} + \text{Cu}$ at PHENIX

Y.-s. Lai (for the PHENIX collaboration)

Columbia University, New York, NY 10027-7061 and Nevis Laboratories, Irvington, NY 10533-2508, USA

The Relativistic Heavy Ion Collider collides heavy nuclei at ultrarelativistic energies, creating a strongly interacting, partonic medium that is opaque to the passage of high energy quarks and gluons. Direct jet reconstruction applied to these collision systems provides a crucial constraint on the mechanism for in-medium parton energy loss and jet-medium interactions. However, traditional jet reconstruction algorithm operating in the large soft background at RHIC give rise to fake jets well above the intrinsic production rate of high- p_T partons, impeding the detection of the low cross section jet signal at RHIC energies. We developed a new jet reconstruction algorithm that uses a Gaussian filter to locate and reconstruct the jet energy. This algorithm is combined with a fake jet rejection scheme that provides efficient jet reconstruction with acceptable fake rate in a background environment up to the central Au + Au collision at $\sqrt{s_{NN}} = 200$ GeV. We present results of its application in $p + p$ and $\text{Cu} + \text{Cu}$ collisions using data from the PHENIX detector, namely $p + p$ cross section, $\text{Cu} + \text{Cu}$ jet yields, the $\text{Cu} + \text{Cu}$ nuclear modification factor, and $\text{Cu} + \text{Cu}$ jet-jet azimuthal correlation.

1. Introduction

Measurements of single particle production at the Relativistic Heavy Ion Collider (RHIC) have found significant suppression in $\text{Cu} + \text{Cu}$ and $\text{Au} + \text{Au}$ collisions at $\sqrt{s_{NN}} = 130$ GeV and $\sqrt{s_{NN}} = 200$ GeV (e.g. [1, 2]). However, single or few-particle observables are fragmentation dependent, and only indirectly probe the energy loss of the parent parton. While direct jet reconstruction has become widely used to study perturbative quantum chromodynamics (PQCD) in e^+e^- and hadronic colliders, the high multiplicity and strongly fluctuating background in heavy ion collisions made direct applications of jet reconstruction difficult.

In PHENIX, the limited detector aperture presents additional difficulty to directly apply traditional jet reconstruction algorithms that are sensitive to large angle fragments (or the lack of such), such as the cone [3] and k_{\perp} algorithms [4, 5]. PHENIX has two “central arm” spectrometers with an aperture consisting of two “arms” with $|\eta| < 0.35$ and $\Delta\phi = \pi/2$ each [6]. Since PHENIX is designed to measure rare and electromagnetic probes, and therefore can sustain a high read-out rate, it is well-suited to measure high- p_T jets at a low cross section. However, the narrow PHENIX central arm aperture especially in $\Delta\eta$ leads to the loss of large angle fragments from jets and potentially larger systematic errors due to the importance of edge effects. With increasing p_T , the fragments of jets become increasingly collimated, with most of the energy concentrated in a cone much smaller than the PHENIX acceptance. A jet reconstruction algorithm that emphasizes the core and deemphasizes the large angle tail would therefore be less sensitive to both the background fluctuation in heavy ion events and the limited aperture of the PHENIX detector.

In order to provide an effective method to reconstruct jets at the presence of heavy ion background and/or limited detector aperture, we started in 2006

to develop a jet reconstruction algorithm that takes advantage of the collimated emission of hadrons and is insensitive to large angle fragments. We observed that the flat weighting in traditional jet reconstruction algorithms makes it prone to large angle fluctuations. While the background grows with R^2 , the jet contribution to the p_T grows slowly above $R \gtrsim 0.3$ (e.g. [7]). A nonflat weighting that enhance the core jet signal to periphery would naturally suppress this sensitivity and stabilize the jet axis. The energy flow variable [8] also provided us with the hint that angular convolution of the event transverse momentum (p_T) density with a continuous distribution can be an effective description of QCD processes. We are therefore using a Gaussian filter as a generalized form of the cone algorithm to reconstruct jets ([9, 10]). Early in the development of jet reconstruction algorithms, the British-French-Scandinavian collaboration used the equivalent to a Gaussian filter with $\sigma = 0.5$ [11], preceding even the Snowmass accord on the cone algorithm [3].

The heavy ion background itself is generated by combination of soft, collective processes, semihard processes and subsequent QCD hadronization. The presence of heavy flavor decays and minijet production suggest that one should expect the background to contain more complex, angularly correlated structures than from a purely randomized and isotropic process. Therefore, a strategy based on statistically subtracting the background would require detailed knowledge about the structure of the heavy ion background and its interaction with the jet reconstruction algorithm.

Fluctuations in the underlying event of heavy ion collisions are known to cause a false apparent jet production, if a jet reconstruction algorithm is applied without proper handling of the background [12]. At the collision energy of RHIC, the intrinsic jet production rate is far below the high- p_T tail of the background fluctuation across a large p_T range that is statistically accessible to RHIC. Based on the $p + p$ jet cross-sections presented later in this pa-

per, we estimate that for the central Cu + Cu at $\sqrt{s_{NN}} = 200$ GeV and p_T between 10–20 GeV/c and 20–30 GeV/c, the jet yields are $N_{\text{evt}}^{-1} dN/dy \approx 4 \times 10^{-3}$ and 8×10^{-5} , respectively, which means that rare fluctuations can contribute significantly to the jet yield, if the background cannot be suppressed below this level. Avoiding the p_T range with background contribution would require measuring jets only at the very end of the p_T range, where the statistics are poor. The presence of rare fluctuations also suggest that a simple removal of low- p_T particles would only sample the stronger fluctuations in the rare, high- p_T tail, while biasing both the fragmentation and energy of the reconstructed jets.

We therefore developed a fake jet rejection strategy that is based on the jet versus background shape and can achieve a higher rejection rate than previously proposed algorithms for the LHC (e.g. [13]). As will be demonstrated below, the fake rejection provides a fast rise to unity efficiency within the RHIC accessible p_T range.

2. Jet reconstruction by Gaussian filtering

It can be shown that the iterative cone algorithm is equivalent to finding local maxima of a filter output in (η, ϕ) with a flat angular weighting $k(r^2) = \theta(R^2 - r^2)$ with $r^2 = \eta^2 + \phi^2$ (note that unlike $k(r^2)$, the filter kernel $h(r^2) \propto -\int dr^2 k(r^2) \propto \max(0, 1 - r^2/R^2)$, and not flat) [14, 15]. The cone algorithm entails a specific choice of angular weighting. The Gaussian filter

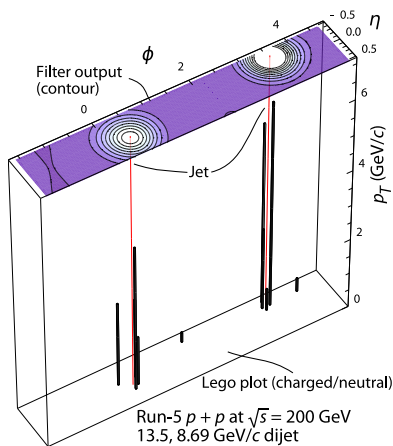


Figure 1: A PHENIX Run-5 $p + p$ at $\sqrt{s} = 200$ GeV dijet event. Charged tracks and photons are shown at the bottom by a Lego plot. The distribution of filter output values of the event is shown at the top as a contour plot. The maxima in the filter density are reconstructed as jet axes, shown as red lines at the positions on the contour and Lego plots.

is based on another, which takes advantage of jets being a collimated emission of particles, and enhances the center of the jet and suppresses the possible contribution from the event background in the periphery. Expressed in the filter form described below, the algorithm samples the entire possible (η, ϕ) range and is seedless. By additionally avoiding a sharp radial cutoff, the algorithm therefore becomes analytically collinear and infrared safe (we also verified the practical infrared safety using a procedure similar to [16]).

A combined event transverse momentum density that contains both the final state particles $p_{T,i}$, and $p_T^{\text{bg}}(\eta, \phi)$, which represents an independently evaluated average contribution from the underlying event, can be defined as

$$p_T(\eta, \phi) = \sum_{i \in F} p_{T,i} \delta(\eta - \eta_i) \delta(\phi - \phi_i) - p_T^{\text{bg}}(\eta, \phi), \quad (1)$$

The Gaussian filtering of p_T is the linear-circular convolution of $p_T(\eta, \phi)$ with a Gaussian distribution

$$p_T^{\text{filt}}(\eta, \phi) = \iint d\eta' d\phi' p_T(\eta', \phi') e^{-((\eta - \eta')^2 + (\phi - \phi')^2)/2\sigma}. \quad (2)$$

The output of the filter for a given (η, ϕ) position is the Gaussian-weighted transverse momentum in that event above the average background from the underlying event. The local maxima in $p_T^{\text{filt}}(\eta, \phi)$ are the reconstructed jets using the Gaussian filter.

Figures 1–2 demonstrate the behavior for a $p + p$ and Cu + Cu event, respectively. Charged tracks and photons are shown at the bottom by a Lego plot. The distribution of filter output values of the event is shown at the top as a contour plot. The maxima in

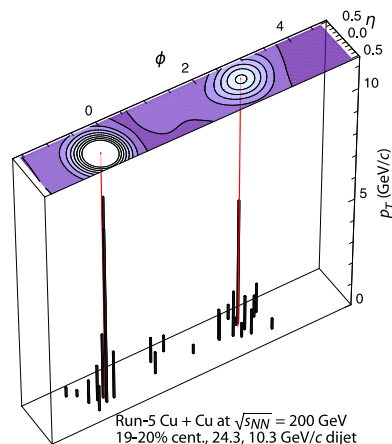


Figure 2: A PHENIX Run-5 Cu + Cu at $\sqrt{s_{NN}} = 200$ GeV dijet event at $\approx 20\%$ centrality. Charged tracks and photons are shown at the bottom by a Lego plot. The distribution of filter output values of the event is shown at the top as a contour plot. The maxima in the filter density are reconstructed as jet axes, shown as red lines at the positions on the contour and Lego plots.

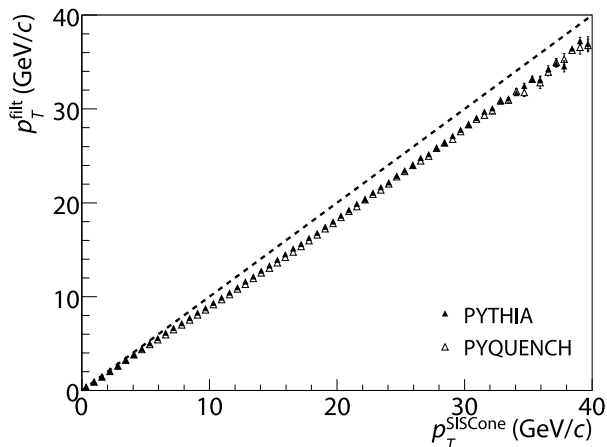


Figure 3: Comparison of the jet energy scale between the $\sigma = 0.3$ Gaussian filter (p_T^{filt}) and the $R = 0.4$ SIS Cone (p_T^{SISCone} , with 0.5 overlap threshold) [16] for $p + p$ collisions at $\sqrt{s} = 200$ GeV using PYTHIA [17] and central Au + Au collisions at $\sqrt{s_{NN}} = 200$ GeV using PYQUENCH [18] at the event generator level (no detector effects). The dashed line indicates the position of $p_T^{\text{filt}} = p_T^{\text{SISCone}}$.

the filter density are reconstructed as jet axes, shown as red lines at the positions on the contour and Lego plots.

The angular weighting of the Gaussian filter modifies the energy summation and therefore will not produce the same jet energy as e.g. the cone algorithm. To evaluate the difference between the energy scales of the $\sigma = 0.3$ Gaussian filter and the $R = 0.4$ SIS Cone algorithms (0.5 overlap threshold) [16], we show in Figure 3 the jet energy scale comparison for both $p + p$ collisions at $\sqrt{s} = 200$ GeV using PYTHIA [17] and central Au + Au collisions at $\sqrt{s_{NN}} = 200$ GeV using PYQUENCH [18] at the event generator level. Further study of its property in $p + p$ events are detailed in [9].

In heavy ion events, the background contribution p_T^{bg} will depend on the collision centrality and reaction plane. The Gaussian filter allows these collision variables to be fully parameterized, which is crucial for heavy ion jet reconstruction algorithm. Due to the narrow pseudorapidity coverage at PHENIX, we also parametrize p_T^{bg} depending on the collision vertex z position. Since in the Cu + Cu system at $\sqrt{s_{NN}} = 200$ GeV, the event-by-event fluctuation strongly dominates over flow effects, we do not parametrize with respect to the reaction plane (note that the linearity in the jet definition means that a weak flow simply translates into an additional p_T smearing).

3. Experimental setup

Figure 4 shows the Run-5 PHENIX central arm configuration for RHIC Run-5 (year 2004/2005). The

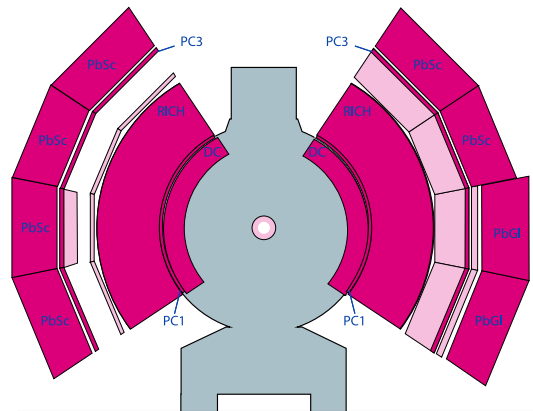


Figure 4: The PHENIX central arm detectors for RHIC Run-5 (year 2004/2005), viewed along the beam axis from the south towards north. Dark regions indicate detectors used for the jet reconstruction: The drift chamber (DC), the pad chamber layers 1 and 3 (PC1/PC3), the ring-imaging Čerenkov detector (RICH), and the Pb scintillator (PbSc) and Pb glass (PbGl) electromagnetic calorimeters.

central arm detectors used for jet reconstruction are the drift chamber (DC), the pad chamber layers 1 and 3 (PC1/PC3), the ring-imaging Čerenkov detector (RICH), and the electromagnetic calorimeters (EMCal). For the data presented in this paper, DC/PC1/PC3 provide momentum measurement for charged particles, and the EMCal the energy for photons and electrons. Two calorimeter technologies were used, 6 of the total 8 sectors are covered by Pb-scintillator (PbSc) EMCal, 2 sectors by Pb-glass (PbGl) calorimeters.

Pattern recognition and momentum reconstruction of the tracking system is performed using a combinatorial Hough transform. The p_T scale is determined by time-of-flight measurement of π^\pm , K^\pm , and p/\bar{p} .

Since PHENIX currently does not have the ability of performing in-field tracking¹, conversion electrons in the DC can produce a displaced track that appears to the momentum reconstruction to be a very high- p_T track originating from the event vertex. Information from the RICH and the dE/dx measurement is therefore used to identify and remove these conversion electrons. To provide additional suppression for jets with $p_T^{\text{rec}} > 20$ GeV/c, we use the fact that conversion electrons are unlikely to angularly coincide with a high- p_T jet, and require the reconstructed jet to have a minimum jet multiplicity of 3 particles, and the charged fraction of the jet p_T to be below 0.9 to remove events with single track and falsely large p_T values.

¹a Si vertex detector upgrade is going to provide such a capability and is scheduled to be installed in year 2010, see e.g. [19]

Shower shape cuts were applied to the EMCal clusters to remove clusters generated by hadronic showers. The absolute energy scale of the calorimeter clusters is determined both by the reconstructed π^0 masses from $\pi^0 \rightarrow \gamma\gamma$ decay, and checked by comparing RICH identified e^\pm momenta from tracking against the corresponding cluster energies. The residual uncertainty in the energy scale is $\pm 3\%$ (syst.).

The PHENIX minimum bias (MB) trigger is defined by the coincident firing of the two beam-beam counters (BBC) located at $3.0 < \eta < 3.9$. The Run-5 BBC cross section is $\sigma_{\text{BBC}} = 22.9 \pm 2.3 \text{ mb}$ (syst.), measured using the Van de Meer/vernier scan method. The efficiency of BBC firing on an event containing a jet with $p_T^{\text{rec}} > 2 \text{ GeV}/c$ is $\epsilon_{\text{BBC}} = 0.86 \pm 0.05$ (syst.) and within that uncertainty, approximately constant with respect to p_T^{rec} . For both our $p + p$ and Cu + Cu measurements, we require the collision vertex to be within $|z| < 25 \text{ cm}$ along the beam axis, derived from the BBC timing information.

All the charge tracks and electromagnetic clusters in the EMCal passing the described cuts are used in the Gaussian filter, and all resulting maxima are considered candidate jets. Since we do not explicitly split jet pairs with small angular separation, it is possible to reconstruct jet pairs with substantial overlap. In reality however, we rarely observe jets reconstructed with an angular separation of $\Delta R < 0.5$.

4. Jet spectrum in $p + p$

The data presented in this section were obtained from the PHENIX $p + p$ dataset from the RHIC Run-5 (year 2004/2005). After removal of bad quality runs, a total of 1.47×10^9 minimum bias $p + p$ and 1.16×10^9 triggered $p + p$ events are being used.

PHENIX can trigger on high- p_T and electromagnetic processes using the central arm EMCal-RICH-trigger (ERT). For the result presented here, we use a trigger that requires a total energy $E > 1.4 \text{ GeV}$ deposited in a 4×4 group of calorimeter towers. This trigger is well-suited for jet measurement due to its low noise level and fast efficiency saturation with respect to the jet p_T . The efficiency is evaluated in term of the p_T^{rec} of the most energetic jet in the event, and rises from approximately 0.25 for $p_T^{\text{rec}} \approx 2.2 \text{ GeV}/c$ to 0.9 for $p_T^{\text{rec}} \approx 9.5 \text{ GeV}/c$. After correction for the efficiency, the minimum bias and triggered datasets agree within an uncertainty of 5% (syst.) in the range from $p_T^{\text{rec}} = 2 \text{ GeV}/c$ up to $30 \text{ GeV}/c$ (limited by the minimum bias data set statistics). Therefore, we calculate a combined jet yield per minimum bias event according to

$$\frac{1}{N_{\text{evt}}} \frac{dN}{dp_T^{\text{rec}}} = \frac{1}{N_{\text{MB}}} \frac{\epsilon_{\text{ERT}}^{-1}(p_T^{\text{rec}}) \frac{dN_{\text{ERT}}}{dp_T^{\text{rec}}} + \frac{dN_{\text{evt}}}{dp_T^{\text{rec}}}}{s_{\text{MB}} + 1}, \quad (3)$$

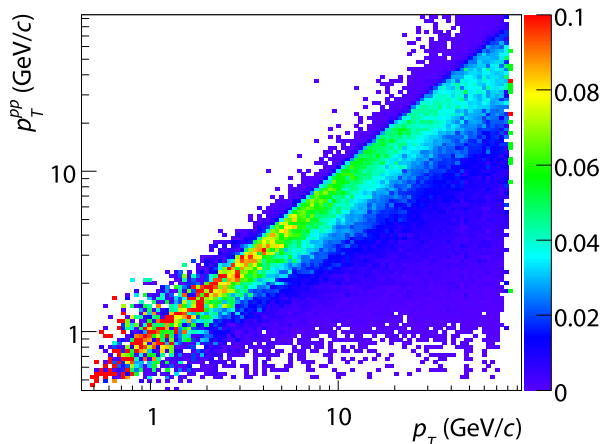


Figure 5: The PHENIX jet $P(p_T^{\text{pp}}|p_T)$ transfer matrix for $\sqrt{s} = 200 \text{ GeV}$ and $\sigma = 0.3$ Gaussian filter, derived from the GEANT simulation of $\approx 1.6 \times 10^7$ PYTHIA events. The $p_T^{\text{pp}} < p_T$ region is dominated by n, K_L^0 energy loss.

where $s_{\text{MB}} = 37.34$ is the average scale down applied to the minimum bias trigger.

The spectrum is then unfolded by the regularized inversion of the Fredholm equation

$$\frac{dN}{dp_T^{\text{rec}}} = \int dp_T P(p_T^{\text{pp}}|p_T) \frac{dN}{dp_T} \quad (4)$$

using singular value decomposition (SVD). The simultaneous minimization of the second order finite-differences is used as a constraint to the continuity of the unfolding result. This procedure is implemented in the software package GURU [20]. The transfer matrix of $P(p_T^{\text{pp}}|p_T)$ expresses the (conditional) probability that a jet with the true transverse momentum, p_T , is reconstructed with p_T^{pp} .

We used PYTHIA 6.4.20 with the (6.4.20-default) “old” multiparton interaction scheme and GEANT simulation to evaluate $P(p_T^{\text{pp}}|p_T)$. A total of 1.6×10^7 events were simulated with 14 different minimum Q^2 settings varying between $\sqrt{Q^2} > 0.5 \text{ GeV}/c$ and $\sqrt{Q^2} > 64 \text{ GeV}/c$. The transfer matrix $P(p_T^{\text{pp}}|p_T)$ resulting from the simulation procedure is shown in figure 5. The $p_T^{\text{pp}} < p_T$ region is dominated by n, K_L^0 energy loss.

We measured the $\sqrt{s} = 200 \text{ GeV}$ $p + p$ spectrum using the combined PHENIX Run-5 minimum bias and triggered data. We require that the reconstructed jet is at least by an angular distance of $d \geq 0.05 \text{ rad}$ inside the infinite momentum PHENIX central arm acceptance. The spectrum with respect to the true p_T is then given by

$$\frac{Ed^3\sigma}{dp^3} = \frac{1}{2\pi p_T} \frac{d^2\sigma}{dp_T dy} = \frac{\sigma_{\text{BBC}}}{A \epsilon_{\text{BBC}}} \frac{1}{p_T} \frac{1}{N_{\text{evt}}} \frac{dN}{dp_T} \quad (5)$$

where dN/dp_T is the unfolding result from (4) and

$$A = 2(\Delta\eta - 2d)(\Delta\phi/2 - 2d) \quad (6)$$

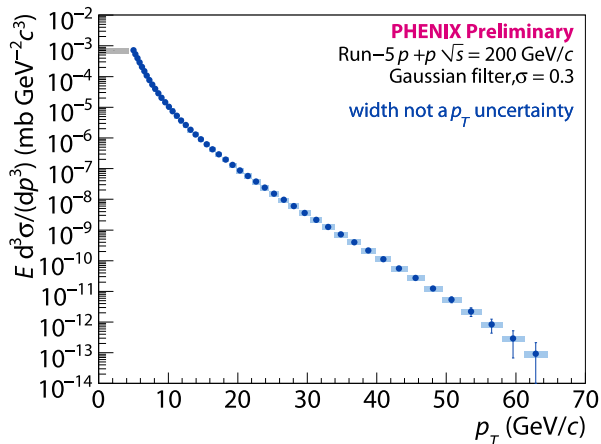


Figure 6: PHENIX Run-5 $p + p$ at $\sqrt{s} = 200$ GeV invariant jet cross section spectrum as a function of p_T . The shaded box to the left indicates the overall normalization systematic uncertainty, shaded boxes associated with data points indicate point-to-point systematic uncertainties, and error bars indicate statistical uncertainties.

the fiducially reduced PHENIX central arm acceptance area.

The regularized least square unfolding involves the regularization parameter τ (or sometimes λ^2) and its choice translates into an uncertainty on the global shape/low frequency component of a jet spectrum. We evaluated the systematic uncertainty in the unfolded spectrum due to such variation in the regularization parameter by varying τ over the entire meaningful range between ≈ 4 degrees of freedom up to the Nyquist frequency. We combine the resulting, point-by-point estimate of the systematic uncertainty for the spectrum shape as part of the total experimental systematic uncertainty. The so evaluated systematic uncertainty is therefore representative of the full range of regularization parameter choices.

The residual $\pm 3\%$ systematic uncertainty in the energy scale translates into a constant uncertainty of $\pm 15\%$ (syst.) for the jet spectrum (due to its power-law shape with largely constant exponent).

Figure 6 shows the PHENIX preliminary $p + p$ jet spectrum measured using the Gaussian filter by the procedures described above, plotted in invariant cross sections. The shaded box to the left indicates the overall normalization systematic uncertainty, shaded boxes associated with data points indicate point-to-point systematic uncertainties, and error bars indicate statistical uncertainties. We show the unfolded spectrum out to the p_T bin where the nominal yield for the number of sampled events reaches the level of 1 jet, namely 60 GeV/c.

Figure 7 shows the same spectrum as in Figure 6, compared against the spectrum from [21], the next-to-leading order (NLO) calculation using the small cone approximation (SCA) [22], and the leading order

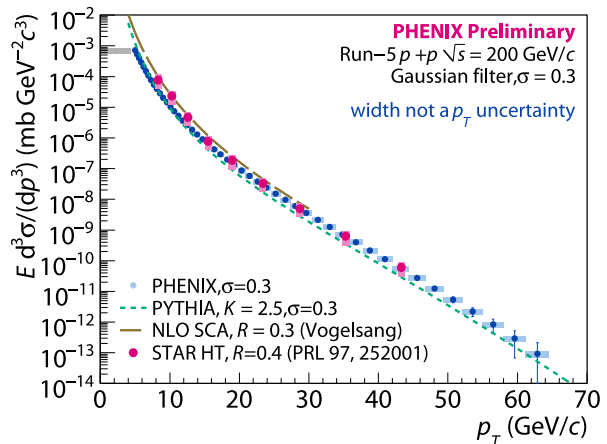


Figure 7: PHENIX Run-5 $p + p$ at $\sqrt{s} = 200$ GeV invariant jet cross section spectrum as a function of p_T , with comparison to [21], next-to-leading order calculation from [22], and PYTHIA assuming $K = 2.5$. The shaded box to the left indicates the overall normalization systematic uncertainty, shaded boxes associated with data points indicate point-to-point systematic uncertainties, and error bars indicate statistical uncertainties.

PYTHIA spectrum assuming $K = 2.5$. The comparison to [21] and NLO SCA involve different jet definitions, a residual difference should be expected, even though for $p_T > 15$ GeV/c it appears to be small between filter and cone jets for the Gaussian size $\sigma = 0.3$ used in this analysis. Our spectrum is close to [21] within its p_T reach. The spectrum also follows approximately the shape of the NLO SCA calculation, and the leading order PYTHIA spectrum, if $K = 2.5$ is assumed. However, a more appropriate comparison would involve Gaussian filter based NLO calculations, which we plan to perform in the future.

5. Cu + Cu results

The data presented in this section were obtained from the PHENIX Cu + Cu dataset from the RHIC Run-5 (year 2004/2005). The $p + p$ data presented above provide a baseline for the Cu + Cu measurements and explicitly appear in the jet nuclear modification factor. After removal of bad quality runs, a total of 1.58×10^8 minimum bias are used in the Cu + Cu analysis, covering the centrality range 0–95%. Because of poor statistics and large uncertainties in the T_{AB} for very peripheral events, we excluded events in the 80–95% centrality range and divide the remainder into 4 bins.

The p_T^{bg} in (1) is parametrized as a product of the centrality and vertex dependent total event p_T^{tot} times a vertex dependent $p_T(\eta, \phi)/p_T^{\text{tot}}$ distribution. The values are estimated by averaging over the minimum bias Cu + Cu events.

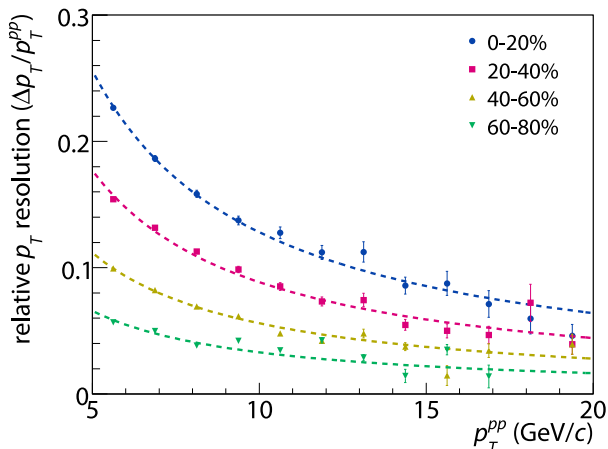


Figure 8: The $\sigma = 0.3$ Gaussian filter p_T resolution with $\Delta p_T/p_T \propto 1/p_T$ (constant energy smearing) fits for different centralities of Cu + Cu collisions at $\sqrt{s_{NN}} = 200$ GeV, evaluated by embedding PHENIX Run-5 $p + p$ events into PHENIX Run-5 Cu + Cu events. The constant energy smearing behavior is expected for an (asymptotically) linear jet reconstruction algorithm.

In heavy ion collisions, centrality-dependent fluctuations in the underlying event will broaden the energy resolution of the jet measurement beyond the detector response described in Section 4. The differences between the Cu + Cu jet p_T scale, p_T^{CuCu} and the $p + p$ energy scale must be accounted for in any comparison of the jet spectra or evaluation of R_{AA} .

We evaluate the effects of the Cu + Cu underlying event on jet measurements by embedding PHENIX-measured $p + p$ events into the minimum bias Cu + Cu events by combining their list of tracks and clusters. We reconstruct the embedded events and evaluate the energy and angular resolution and the reconstruction efficiency for jets that match the input $p + p$ jets within a radial separation $\Delta R < 0.3$. Both events are required to fall into the same $\Delta z = 5$ cm bin in vertex position. The evaluated transfer matrix is then recombined into the final centrality binning using N_{coll} scaling. Due to the linearity of Gaussian filter, for $p_T^{pp} > 8$ GeV/c the energy smearing is constant within our statistical uncertainty. We use this feature of the energy response to extend the transfer matrix to higher p_T where the limited statistics in the $p + p$ sample would otherwise introduce fluctuations into the transfer matrix that would have a negative impact on the unfolding.

Figure 8 shows the $\sigma = 0.3$ Gaussian filter p_T resolution for different centralities of Cu + Cu collisions at $\sqrt{s_{NN}} = 200$ GeV, evaluated by embedding PHENIX Run-5 $p + p$ events into PHENIX Run-5 Cu + Cu events. Superimposed are $\Delta p_T/p_T \propto 1/p_T$ fits that shows the constant energy smearing, which is expected for an (asymptotically) linear jet reconstruction algorithm such as the Gaussian filter.

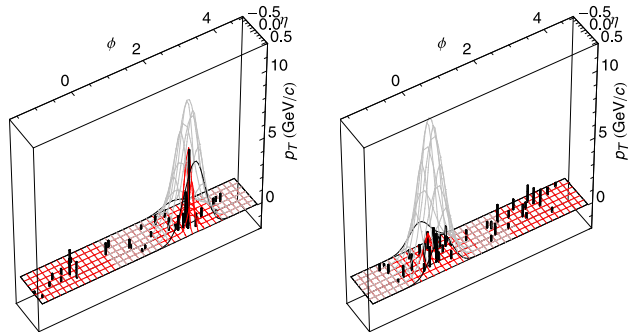


Figure 9: Comparison between a PHENIX Run-5 Cu + Cu event with a 9.6 GeV/c jet passing fake rejection and an event with 10.8 GeV/c “jet” that fails the fake rejection, and is presumed to be a background fluctuation

Due to the large N_{coll} in central Cu + Cu events, the underlying event has potentially a high yield to contain an intrinsic jet. This is avoided by requiring that reconstructed jet after embedding matches a $p + p$ jet with $p_T^{pp} > 4$ GeV/c within an angular range of $\Delta R < 0.3$. The residual contamination was evaluated by reconstructing the underlying event jet spectrum within ΔR of the original $p + p$ jet axis, and is found to be $< 10^{-2}$.

In the measurement presented here, we use two approaches to correct for the energy scale difference in Cu + Cu collisions: (a) by unfolding the Cu + Cu spectrum using the transfer matrix $P(p_T^{\text{CuCu}}|p_T^{pp})$, the R_{AA} is then calculated by comparing against the $p + p$ spectrum; and (b) by embedding $p + p$ events into Cu + Cu events, so that the $p + p$ spectra attains the Cu + Cu background induced energy smearing, and the R_{AA} is derived by comparing the Cu + Cu spectrum to the embedded spectrum.

5.1. Fake jet rejection

In order to reduce the contribution of fake jets, we apply a shape based discriminant to the jets. The discriminant is defined as

$$g_{\sigma_{\text{dis}}}(\eta, \phi) = \sum_{i \in \text{fragment}} p_{T,i}^2 e^{-((\eta_i - \eta)^2 + (\phi_i - \phi)^2)/2\sigma_{\text{dis}}}, \quad (7)$$

where (η, ϕ) is the reconstructed jet axis. The discriminant size $\sigma_{\text{dis}} = 0.1$ to chosen to be approximately or below the size $\Delta R^{\text{bg}} = \sqrt{2\pi/(dN/d\eta)}$, which is the characteristic background particle separation. If the local distribution of high- p_T particle indicates that the jet may be misreconstructed in its angle (e.g. a background fluctuation beneath the jet with a nonzero gradient), we also search for an (η, ϕ) where $g_{\sigma_{\text{dis}}}$ might be maximized. We denote this “adapted” discriminant $g'_{\sigma_{\text{dis}}}$. In HIJING studies, we found this discriminant, when applied to central

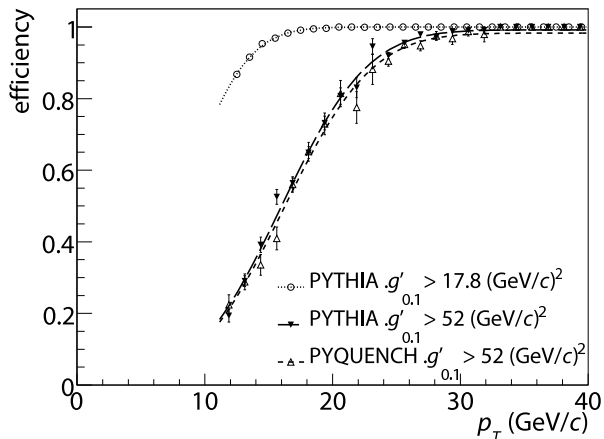


Figure 10: Efficiency for the $g'_{0.1} > 52 \text{ (GeV/c)}^2$ fake jet rejection that is suitable for central Au + Au collisions at $\sqrt{s_{NN}} = 200 \text{ GeV}$ for $p + p$ collisions at $\sqrt{s} = 200 \text{ GeV}$ using PYTHIA [17] and central Au + Au collisions at $\sqrt{s_{NN}} = 200 \text{ GeV}$ using PYQUENCH [18] at the event generator level (no detector effects), compared to the PYTHIA efficiency for $g'_{0.1} > 17.8 \text{ (GeV/c)}^2$ that is used for Cu + Cu collisions.

Au + Au collisions at RHIC, to significantly outperform discriminants proposed for the LHC, such as the $p_T/\langle A \rangle$ [23] or Σj_T [13].

Figure 9 illustrates the behavior of the fake jet rejection using two actual PHENIX Run-5 Cu + Cu events.

With the definition in (7), it is also possible to achieve a largely centrality independent efficiency turn-on. This feature is important in order to constrain the systematic impact in a centrality dependent measurement. We could, in principle, adapt the fake rejection to the collision centrality but that by keeping the rejection threshold fixed we obtain a nearly centrality independent jet finding efficiency. Using the studies of the discriminant distribution in Cu + Cu collisions and on the dijet $\Delta\phi$ analysis presented below, we have chosen a nominal discriminant threshold of $g'_{0.1} > 17.8 \text{ (GeV/c)}^2$.

There are several methods to investigate the sensitivity of reconstructed jets to the fake rejection. The discriminant distribution shows that for $p_T > 16 \text{ GeV/c}$, the jets have discriminant values that lie mostly above our Cu + Cu fake jet rejection threshold of $g'_{\text{dis}} > 17.8 \text{ (GeV/c)}^2$. Changing or removing the threshold therefore has little impact on our spectra and R_{AA} above 12–16 GeV/c .

We further studied the sensitivity of both efficiency after fake jet rejection and the energy scale using PYTHIA and PYQUENCH at the fake jet rejection level $g'_{0.1} > 52 \text{ (GeV/c)}^2$ required for central Au + Au collisions at $\sqrt{s_{NN}} = 200 \text{ GeV}$. Both the efficiency and the jet energy scale compared to SIScone shows very small modification, i.e. below the present systematic uncertainty in the overall energy scale. This is shown in Figure 10, and the comparison between

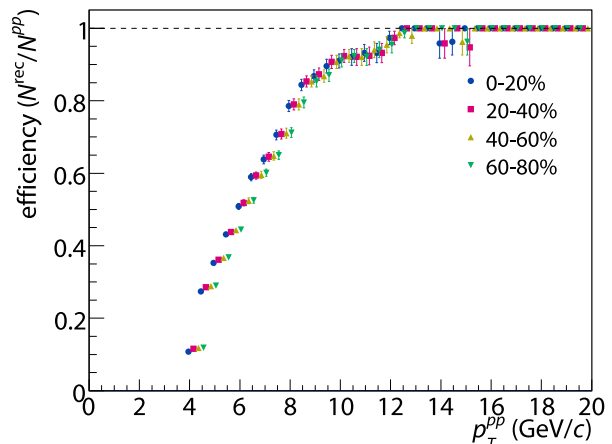


Figure 11: Efficiency for the $g'_{0.1} > 17.8 \text{ (GeV/c)}^2$ fake jet rejection for different centralities of Cu + Cu collisions at $\sqrt{s_{NN}} = 200 \text{ GeV}$, evaluated by embedding PHENIX Run-5 $p + p$ events into PHENIX Run-5 Cu + Cu events

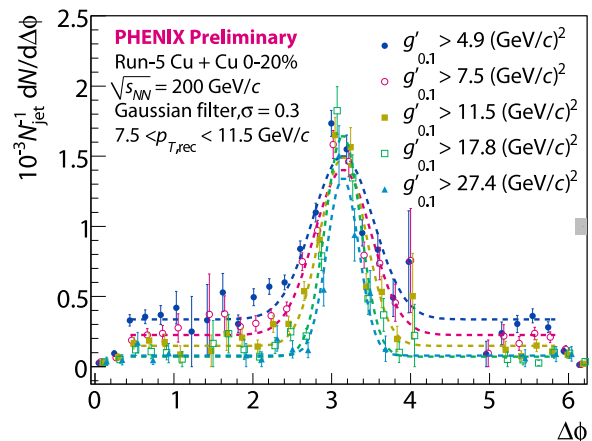


Figure 12: Run-5 Cu + Cu at $\sqrt{s_{NN}} = 200 \text{ GeV}$ azimuthal correlation for 0–20% centrality dijets in yields and with different $g'_{0.1}$ fake jet rejection thresholds. The nominal fake jet rejection threshold used is $g'_{0.1} > 17.8 \text{ (GeV/c)}^2$.

PYTHIA and PYQUENCH jet energy scales was shown in Figure 3. Figure 11 shows the efficiency for the $g'_{0.1} > 17.8 \text{ (GeV/c)}^2$ fake rejection for different centralities of Cu + Cu collisions at $\sqrt{s_{NN}} = 200 \text{ GeV}$.

Angular correlation of dijets can be used to study the yield of residual fake jets. The yield of three and more jets at large angle with respect the leading dijet axis (e.g. due to multiple collisions or initial and final state radiation) is strongly suppressed at high- p_T , and therefore the decorrelated yield approximately perpendicular to the dijet axis is a good estimator of the residual contamination by fake jets. In the Cu + Cu data, the $\Delta\phi$ distribution saturates at our normal discriminant threshold of $g'_{0.1} > 17.8 \text{ (GeV/c)}^2$. At $p_T^{\text{CuCu}} \approx 7.5 \text{ GeV/c}$ for 0–20% centrality, this translates into an upper bound of 10% for the fake jet con-

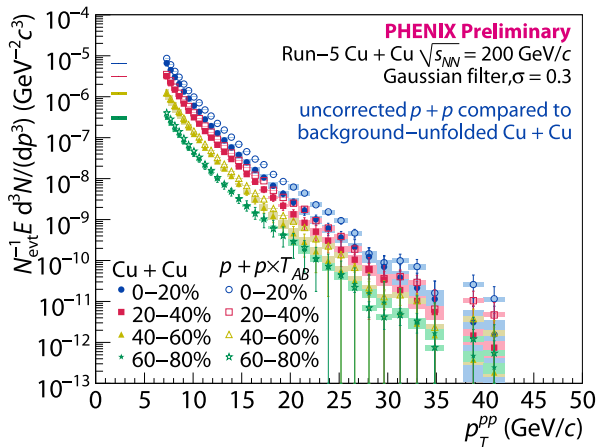


Figure 13: PHENIX Run-5 Cu + Cu at $\sqrt{s_{NN}} = 200$ GeV invariant jet yield as function of p_T^{pp} , with comparison to the $\langle T_{AB} \rangle$ scaled $p + p$ cross section. The shaded box to the left indicates the centrality-dependent systematic uncertainty in the normalization, shaded boxes associated with data points indicate point-to-point systematic uncertainties, and error bars indicate statistical uncertainties.

tamination in the jet yield. Figure 12 shows the effect of the increasing fake jet rejection on the $\Delta\phi$ distribution using the 0–20% centrality Run-5 Cu + Cu data.

5.2. Cu + Cu jet spectra and nuclear modification factors

We unfold the raw spectrum dN/dp_T^{CuCu} using the centrality dependent transfer matrix $P(p_T^{CuCu}|p_T^{pp})$ and obtain the spectrum in term of the dp_T^{pp} energy scale, dN/dp_T^{pp} . The invariant yield in the respective p_T scale is then given by

$$\frac{1}{N_{\text{evt}}} \frac{E d^3 N}{dp^3} = \frac{1}{\epsilon_{\text{fr}}(p_T)} \frac{1}{A} \frac{1}{p_T} \frac{1}{N_{\text{evt}}} \frac{dN}{dp_T}, \quad (8)$$

with the same fiducially reduced area A defined in (6), and where ϵ_{fr} is the fake rejection efficiency (compare figure 11). For both the jet spectra and R_{AA} measurement, we conservatively restrict our p_T range to the region with $\epsilon_{\text{fr}} > 0.75$. When applying the charged fraction cut in Cu + Cu events, we only include particles with $p_T > 1.5$ GeV/c, so that background fluctuations cannot cause us to accept fake jets generated by late conversion electrons.

Figure 13 shows the invariant jet yield as function of p_T^{pp} together with the $\langle T_{AB} \rangle$ scaled $p + p$ cross section, where T_{AB} is the nuclear overlap function with Cu + Cu values given in [2] are used. The shaded box to the left indicates the centrality-dependent systematic uncertainty in the normalization, shaded boxes associated with data points indicate point-to-point systematic uncertainties, and error bars indicate statistical uncertainties.

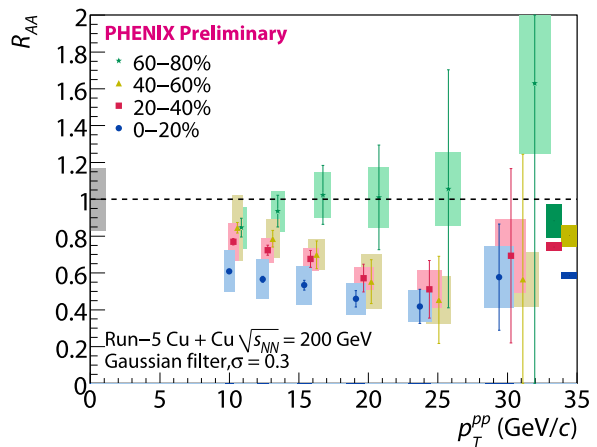


Figure 14: PHENIX Run-5 Cu + Cu at $\sqrt{s_{NN}} = 200$ GeV R_{AA} derived from unfolding. The shaded box to the left indicates the $p + p$ -Cu + Cu systematic uncertainty in the jet energy scale, shaded boxes to the right shows centrality dependent systematic uncertainty between embedding and unfolding, shaded boxes associated with data points indicate point-to-point systematic uncertainties, and error bars indicate statistical uncertainties.

The nuclear modification factor is defined by

$$R_{AA} = \frac{N_{\text{evt}}^{-1} dN_{\text{CuCu}}/dp_T}{\langle T_{AB} \rangle d\sigma_{pp}/dp_T}. \quad (9)$$

For the R_{AA} in p_T^{pp} energy scale and using unfolding, we divide the spectra shown in Figure 13 by the raw $p + p$ spectrum in p_T^{pp} .

To check for potential systematic errors resulting from the unfolding, we alternatively evaluated the R_{AA} by comparing the raw Cu + Cu spectrum to the embedded $p + p$ spectrum. Since the extracted R_{AA} do not show a significant p_T dependence within the uncertainties, we can compare between the two sets of R_{AA} despite the difference in the jet energy scale. We additionally studied the sensitivity of the R_{AA} to vertex and fiducial cuts. The so evaluated, centrality dependent differences from the unfolding/embedding comparison, vertex dependence, fiducial dependence, are combined to obtain the centrality dependent systematic uncertainties.

Figure 14 shows the extracted R_{AA} using unfolding. The shaded box to the left indicates the $p + p$ -Cu + Cu systematic uncertainty in the jet energy scale, shaded boxes to the right shows centrality dependent systematic uncertainty between embedding and unfolding, shaded boxes associated with data points indicate point-to-point systematic uncertainties, and error bars indicate statistical uncertainties.

Figure 15 shows the comparison between the R_{AA} derived using unfolding and embedding (with the same notation as in Figure 14). The level of the suppression obtained with both methods is the same within the statistical and unfolding-systematic uncer-

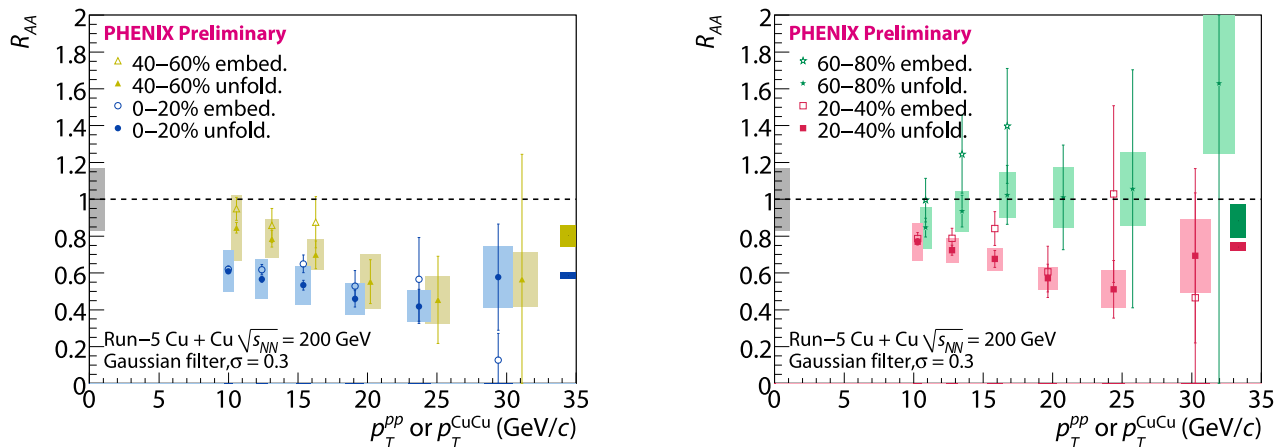


Figure 15: Comparison between the PHENIX Run-5 Cu + Cu at $\sqrt{s_{NN}} = 200$ GeV R_{AA} derived from unfolding (filled symbols) and embedding (open symbols). The shaded box to the left indicates the $p + p$ -Cu + Cu systematic uncertainty in the jet energy scale, shaded boxes to the right shows centrality dependent systematic uncertainty between embedding and unfolding, shaded boxes associated with data points indicate point-to-point systematic uncertainties, and error bars indicate statistical uncertainties. Note that the flatness of R_{AA} makes a comparison across different energy scales possible.

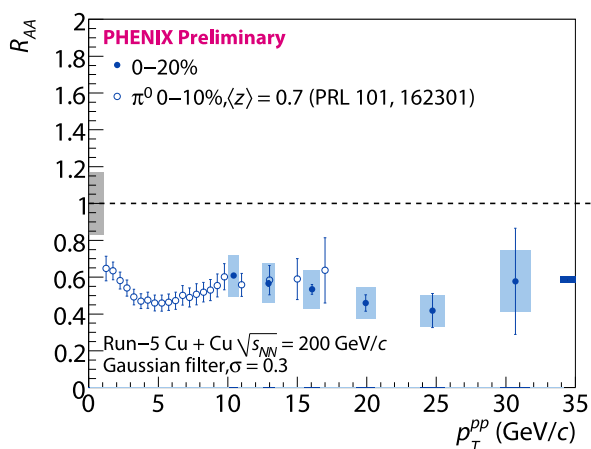


Figure 16: Comparison between the central PHENIX Run-5 Cu + Cu at $\sqrt{s_{NN}} = 200$ GeV jet R_{AA} derived from unfolding and the π^0 R_{AA} . The shaded box to the left indicates the $p + p$ -Cu + Cu systematic uncertainty in the jet energy scale, shaded boxes to the right shows centrality dependent systematic uncertainty between embedding and unfolding, shaded boxes associated with data points indicate point-to-point systematic uncertainties, and error bars indicate statistical uncertainties. Note that while the flatness of R_{AA} makes a comparison across different energy scales possible, π^0 with $\langle z \rangle = 0.7$ has a different energy scale.

tainties, which gives us confidence that the unfolding procedure is not significantly biasing the result. Figure 16 compares the central 20% suppression with the π^0 suppression from [2] (with the same notation as in Figure 15). While the R_{AA} of π^0 has a different energy scale than jets, both R_{AA} are approximately flat with respect to p_T within our accessible range and

Centrality	Width
0–20%	0.223 ± 0.017
20–40%	0.231 ± 0.016
40–60%	0.260 ± 0.059
60–80%	0.253 ± 0.055

Table I Widths of Gaussian fit to the PHENIX Run-5 Cu + Cu at $\sqrt{s_{NN}} = 200$ GeV azimuthal angular correlation for jets with $7.5 \text{ GeV}/c < p_T^{\text{CuCu}} < 11.5 \text{ GeV}/c$

therefore allows a comparison.

We observe a R_{AA} that becomes gradually suppressed with increasing centrality. The level of suppression in the most central 20% centralities is at $R_{AA} \approx 0.5$ –0.6 and comparable to that of π^0 .

5.3. Cu + Cu jet-jet azimuthal correlations

The Cu + Cu jet-jet azimuthal correlation is extracted by correcting for the acceptance effect using the area-normalized mixed event yield (e.g. [24]):

$$\frac{dN(\Delta\phi)}{d\Delta\phi} = \frac{1}{A(\Delta\phi)} \frac{dN^{\text{raw}}(\Delta\phi)}{d\Delta\phi} \quad (10)$$

where $A(\Delta\phi)$ is the detector acceptance correction. Using a Gaussian fit to the distribution, we extracted the width for $7.5 \text{ GeV}/c < p_T^{\text{CuCu}} < 11.5 \text{ GeV}/c$. The widths are consistent within the uncertainty across all centrality ranges.

Figure 17 shows the azimuthal jet-jet correlation with Gaussian fits for jets with $7.5 \text{ GeV}/c < p_T^{\text{CuCu}} < 11.5 \text{ GeV}/c$. Table I lists the Gaussian widths ex-

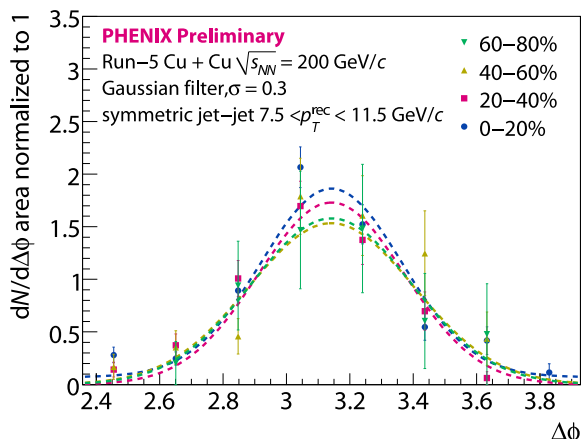


Figure 17: PHENIX Run-5 Cu + Cu at $\sqrt{s_{NN}} = 200$ GeV azimuthal jet-jet correlation with Gaussian fits for jets with $7.5 \text{ GeV}/c < p_T^{\text{CuCu}} < 11.5 \text{ GeV}/c$

tracted from the azimuthal jet-jet correlation for jets with $7.5 \text{ GeV}/c < p_T^{\text{CuCu}} < 11.5 \text{ GeV}/c$.

6. Discussion

Using the PHENIX Run-5 $p + p$ dataset, we extracted the first RHIC $p + p$ spectrum that extends to $p_T \approx 60 \text{ GeV}/c$ or $Ed^3\sigma/dp^3 \approx 0.3 \text{ fb GeV}^{-2}c^3$. This effectively demonstrates the capability of PHENIX as a detector for the study of jet physics.

Applying our algorithm to Cu + Cu collisions, we were also able to clearly demonstrate, for the first time, the feasibility of direct jet reconstruction in heavy ion collisions and for all centralities. We are able to show the centrality dependent onset of jet suppression from peripheral to central collision. This demonstrates the capability of the Gaussian filter algorithm as a heavy ion jet reconstruction algorithm, that can be applied, fully unconstrained, in any heavy ion collision setting at RHIC.

Our $\sigma = 0.3 R_{AA}$ in Cu + Cu suggest that the jet production is strongly suppressed, and is comparable to the suppression level of high- $p_T \pi^0$. Strong suppression in reconstructed jets indicate that significant amount of energy disappears from the angular region covered by the size of the jet reconstruction algorithm. Since the fake jet rejection has little impact on jets with $p_T > 12\text{--}16 \text{ GeV}/c$, we observe an overall suppression that is independent from the fake rejection scheme. However, if jets significantly broadens at the presence of the medium, it is possible that small angle jet reconstruction algorithm such as the $\sigma = 0.3$ Gaussian filter is deselecting these jets. We are current pursuing jet spectra and R_{AA} evaluation with larger angle to address this.

The azimuthal correlation suggest that the surviving parton traversing the medium has very small

transverse k_T broadening.

While our current results are encouraging and demonstrates the accessibility of a large inventory of heavy ion jet variables to PHENIX, we would have to continue our measurement in term of fragmentation properties and jet angular size dependence to understand and complete our picture of the parton energy loss. Since our $p + p$ results probes in a previously unreached RHIC kinematic range, additional comparisons with PQCD calculations could also provide valuable insights.

References

- [1] K. Adcox et al., Phys. Rev. Lett. **88**, 022301 (2001).
- [2] A. Adare et al., Phys. Rev. Lett. **101**, 162301 (2008).
- [3] J. E. Huth et al., in *Research directions for the decade: proceedings of the 1990 Summer Study on High Energy Physics* (1990), pp. 134–136.
- [4] S. Catani, Y. L. Dokshitzer, and B. R. Webber, Phys. Lett. B **285**, 291 (1992).
- [5] S. D. Ellis and D. E. Soper, Phys. Rev. D **48**, 3160 (1993).
- [6] K. Adcox et al., Nucl. Instrum. Methods A **499**, 469 (2003).
- [7] D. Acosta et al., Phys. Rev. D **71**, 112002 (2005).
- [8] C. F. Berger, T. Kúcs, and G. Sterman, Phys. Rev. D **68**, 014012 (2003).
- [9] Y.-s. Lai and B. A. Cole (2008), arXiv:0806.1499.
- [10] Y.-s. Lai (2009), arXiv:0907.4725.
- [11] M. G. Albrow et al., Nucl. Phys. B **160**, 1 (1979).
- [12] C. Stewart et al., Phys. Rev. D **42**, 1385 (1990).
- [13] N. Grau, Eur. Phys. J. C **62**, 191 (2009).
- [14] Y.-z. Cheng, IEEE Trans. Pattern Anal. Mach. Intell. **17**, 790 (1995).
- [15] M. Fashing and C. Tomasi, IEEE Trans. Pattern Anal. Mach. Intell. **27**, 471 (2005).
- [16] G. P. Salam and G. Soyez, J. High Energy Phys. **2007**, 086 (2007).
- [17] T. Sjöstrand, S. Mrenna, and P. Skands, J. High Energy Phys. **2006**, 026 (2006).
- [18] I. P. Lokhtin and A. M. Snigirev, Eur. Phys. J. C **45**, 211 (2005).
- [19] J. M. Heuser, Nucl. Instrum. Methods A **511**, 210 (2003).
- [20] A. Höcker and V. Kartvelishvili, Nucl. Instrum. Methods A **372**, 469 (1996).
- [21] B. I. Abelev et al., Phys. Rev. Lett. **97**, 252001 (2006).
- [22] B. Jäger, M. Stratmann, and W. Vogelsang, Phys. Rev. D **70**, 034010 (2004).
- [23] M. Cacciari and G. P. Salam, Phys. Lett. B **659**, 119 (2008).
- [24] S. S. Adler et al., Phys. Rev. Lett. **97**, 052301 (2006).